Journal of Alloys and Compounds 509 (2011) 9924–9929

Contents lists available at ScienceDirect

Journal of Alloys and Compounds

journal homepage: www.elsevier.com/locate/jallcom

Morphology and phase evolvement of Yb^{3+}/Er^{3+} co-doped $NaYF_4$ microtubes prepared with YF_3 submicrospindles as precursor

Yue Tian[a,b], Ruinian Hua[a,*], Naisen Yu[c], Wei Zhang[a], Liyan Na[a], Baojiu Chen[b,*]

[a] College of Life Science, Dalian Nationalities University, Dalian, Liaoning 116600, PR China
[b] Department of Physics, Dalian Maritime University, Dalian, Liaoning 116026, PR China
[c] College of Physics and Materials Engineering, Dalian Nationalities University, Dalian, Liaoning 116600, PR China

ARTICLE INFO

Article history:
Received 7 June 2011
Received in revised form 24 July 2011
Accepted 25 July 2011
Available online 3 August 2011

Keywords:
$NaYF_4$ microtubes
Hexagonal phase
Controllable synthesis
Upconversion
Energy transfer

ABSTRACT

Hexagonal phase $NaYF_4$ microtubes co-doped with Yb^{3+} and Er^{3+} were synthesized through a hydrothermal process with YF_3 submicrospindles as precursor. The X-ray powder diffraction (XRD), field emission scanning electron microscopy (FE-SEM), transmission electron microscopy (TEM) and high resolution transmission electron microscopy (HRTEM) were utilized to characterize the structure and morphology of the as-prepared products. XRD results show that pure cubic $NaYF_4$ crystals can be obtained when reaction time is 2 h. While the product is mixture of cubic and hexagonal phase $NaYF_4$ when reaction time is from 7 to 20 h. Continuing to increase the reaction time to 24 h, the pure hexagonal $NaYF_4$ crystals were formed. The FE-SEM and TEM results show that the morphology of pure cubic $NaYF_4$ is spherical clusters composed of spherical nanoparticles with average diameter of about 100 nm and the pure hexagonal $NaYF_4$ crystals have tubular structure with out diameter of about 0.3–0.5 μm, inner diameter of about 0.5–1 μm and length ranging from 3 to 12 μm. The luminescence properties of Yb^{3+}/Er^{3+} co-doped cubic and hexagonal phase $NaYF_4$ microcrystals were also studied. Under 980-nm excitation, the upconversion luminescence (UCL) intensity of hexagonal phase $NaYF_4$ microtubes is much stronger than that of cubic phase clusters. Moreover, both red and green upconversion are ascribed to the two-photon process. Therefore, hexagonal phase $NaYF_4$ microtubes with high UCL efficiency may have a potential application in photonic device.

1. Introduction

It is well known that the physical and chemical properties of inorganic crystals are directly related with their dimensions, sizes and morphologies [1]. Therefore, inorganic materials with novel morphologies have attracted considerable interest during the past decade owing to their potential in fundamental studies and technological applications [2–5]. By far, plenty of efforts have been devoted to the fabrication of various kinds of inorganic materials with different shapes and sizes [6–11]. At present, many efficient approaches involving ionic liquid, arc discharge, laser ablation, and biotemplate, as well as template-directed methods have been developed for the preparation of nano-/micro-crystals [12–16]. Nevertheless, the above-mentioned routes call for some special instruments or harsh conditions, and usually lead to impurities because of the incomplete removal of the templates. By contrast, hydrothermal synthesis, which is a more promising technique than conventional methods in terms of cost and potential for large scale production, is considered as one of the useful ways to prepare novel nano-/micro-structured inorganic materials.

Rare earth compounds, such as oxides, phosphates, fluorides, vanadates, tungstates and molybdates have been extensively studied owing to their potential applications in high performance magnets, luminescent devices, catalysts, and other functional materials based on the electronic, optical, and chemical characteristics arising from the 4f electrons of rare earth ions [10,17–22]. Among these compounds, rare earth fluorides evoke more attention because of their unique properties including high refractive index and low phonon energy. Furthermore, fluorides exhibit adequate thermal and environmental stability and are regarded as excellent host lattices for down-conversion (DC) and up-conversion (UC) luminescence of lanthanide ions [23,24]. The DC process is the conversion of higher-energy photons into lower-energy photons, which is also extensively exploited in semiconductor quantum dots and organic dyes. By contrast, UC process is the generation of higher-energy photons from lower-energy radiation on the basis of sequential adsorption and energy-transfer steps. The UC of infrared to visible light by materials doped with rare earth ions has attracted considerable attention due to the potential applications in the areas of color display, short wavelength lasers and

* Corresponding authors. Tel.: +86 411 87633470.
E-mail addresses: rnhua@dlnu.edu.cn (R. Hua), chenmbj@sohu.com (B. Chen).

0925-8388/$ – see front matter © 2011 Elsevier B.V. All rights reserved.
doi:10.1016/j.jallcom.2011.07.095

biomedicine. Among these rare earth ions, the Er^{3+} ion, which has several metastable energy levels and can restore the excitation energy for up-converting near infrared (NIR) light into short wavelength radiation, is a very excellent candidate for UCL [25]. However, the absorption across section of Er^{3+} is narrow in near infrared region, which leads to that the luminescent efficiency of Er^{3+} single doped materials is relatively low. In order to increase UCL efficiency, the Yb^{3+} ion is usually introduced as a sensitizer due to the large absorption across section in the near infrared region. Therefore, the Yb^{3+}/Er^{3+} ion pairs have been studied extensively for achievement of frequency UCL under different pumping excitation wavelength in various hosts, such as glasses, glass ceramics, phosphors, etc. [26–30]. Accordingly, many mechanisms for UCL processes have been proposed. To date, $NaYF_4$ is acknowledged as the most efficient UC host material because of lower phonon energy, adequate chemical and physical stability, etc. [31]. The crystal structure of $NaYF_4$ exhibits two polymorphic forms, namely, cubic (α) and hexagonal (β) phases, depending on the synthesis conditions and methods. Moreover, it was reported that the UCL in Yb^{3+}/Er^{3+} doped $NaYF_4$ strongly depends on the phase and particle size [31]. For example, compared with the cubic sample, the UCL efficiency of green emission in hexagonal $NaYF_4$:Yb^{3+}, Er^{3+} is about 10 times stronger than that of cubic $NaYF_4$:Yb^{3+}, Er^{3+} [31]. Consequently, how to obtain the pure hexagonal phase of $NaYF_4$ is the key in successfully achieving a brighter UC phosphor.

Recently, it was reported that inorganic materials with hollow interiors have a potential application in photonic devices [32]. Accordingly, the controlled synthesis of inorganic materials with tubular structure is necessary for this application. Up to now, many inorganic nanotubes such as sulfides, nitrides, oxides, and fluoride have been reported [33–37]. However, there are no reports on the study of hollow $NaYF_4$ with micrometer size. It is well known that the luminescent efficiency of micrometer sized phosphors is higher than that of corresponding nanomaterials. Therefore, in order to further exploit $NaYF_4$ for application in photonic devices, the synthesis of hollow interiors $NaYF_4$ microtubes is a very significant work.

Taking into account the above reasons, we synthesized $NaYF_4$:Yb^{3+}, Er^{3+} microtubes via hydrothermal process with YF_3:Yb^{3+}, Er^{3+} submicrospindles as precursor in this work. The whole synthesis processes were taken in the aqueous environment without the aid of any templates or surfactants. It is found that the time of hydrothermal treatment plays an important role in the evolvement of morphology and phase of the final product. In addition, The UCL properties of products were also studied in details.

2. Experimental

2.1. Materials

All the chemical reagents used in this study were analytically pure grade without further purification. The rare earth oxides including Y_2O_3 (99.999%), Er_2O_3 (99.999%) and Yb_2O_3 (99.999%) were purchased from Shanghai Second Chemical Reagent Factory (China). NaF was purchased from Beijing Chemical Corporation (China). $Y(NO_3)_3{\cdot}6H_2O$, $Yb(NO_3)_3{\cdot}6H_2O$ and $Er(NO_3)_3{\cdot}6H_2O$ powders were obtained by dissolving the corresponding rare earth oxide in 6 mol/L of nitric acid and recrystallizing for four times.

2.2. Preparation of spindle-like YF_3:10%Yb^{3+}, 2%Er^{3+}

YF_3:10%Yb^{3+}, 2%Er^{3+} submicrospindles were prepared via a facile sonochemical route from an aqueous solution of $Y(NO_3)_3{\cdot}6H_2O$, $Yb(NO_3)_3{\cdot}6H_2O$, $Er(NO_3)_3{\cdot}6H_2O$ and NaF. The detailed procedure is described as follows. First, $Y(NO_3)_3{\cdot}6H_2O$, $Yb(NO_3)_3{\cdot}6H_2O$, $Er(NO_3)_3{\cdot}6H_2O$ were weighed according to the molar ratio of 1:0.1:0.02 and dissolved in 60 mL distilled water under vigorous stirring until they were dissolved completely. Secondly, 0.5 mol/L NaF aqueous solution was dropped slowly in rare earth nitrate solution. Thirdly, The resulting mixture was ultrasonically irradiated with a high-intensity probe (JiNing Co.; 0.6 cm diameter; Ti-horn; 600 W), which was immersed directly in the reaction solution, and the total reaction time was 30 min. The white precipitates were collected by centrifuging at 8000 rpm and washed with distilled water. The YF_3:10%Yb^{3+}, 2%Er^{3+} powders were obtained after the precipitates were dried in vacuum condition at 80 °C for 10 h.

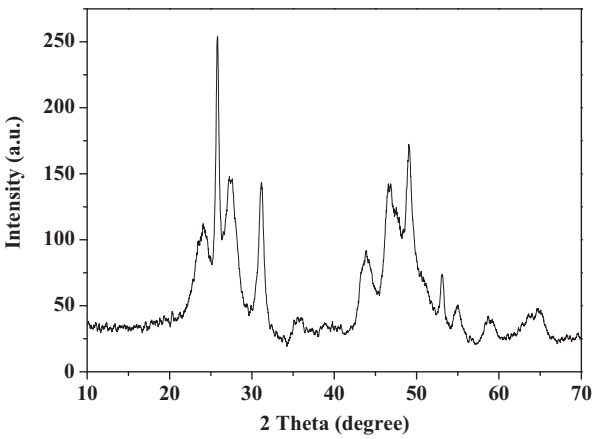

Fig. 1. XRD pattern of the YF_3:10%Yb^{3+}/2%Er^{3+} precursor prepared via sonochemical route.

2.3. Preparation of hexagonal phase $NaYF_4$:10%Yb^{3+}, 2%Er^{3+} microtubes

Hexagonal phase $NaYF_4$:10%Yb^{3+}, 2%Er^{3+} microtubes were prepared via a hydrothermal process by use of YF_3:10%Yb^{3+}, 2%Er^{3+} submicrospindles as precursor solution. In a typical procedure, the precursor solution of YF_3:10%Yb^{3+}, 2%Er^{3+} prepared through sonochemical route was directly transferred into 100 mL Teflon bottle held in a stainless steel autoclave, which was sealed and maintained at 200 °C for 24 h. As the autoclave was cooled to room temperature naturally, the precipitates were separated by centrifugation, washed with distilled water, and then dried in air at 80 °C for 12 h. In order to study the effect of reaction time on the structure, morphology of the product, the time-dependent experiment was performed.

2.4. Characterization

X-ray powder diffraction (XRD) was carried out on a Shimadzu XRD-6000 diffractometer with CuKα_1 radiation (λ = 0.15406 nm). The XRD data were collected by using a scanning mode in the 2θ ranging from 10° to 70° with a scanning step size of 0.02° and a scanning rate of 4.0° min^{-1}. FE-SEM images were obtained using a Hitachi S-4800 field emission scanning electron microscopy operating at acceleration voltage of 5 kV. The low- and high-resolution transmission electron microscope (HRTEM) images were performed using a JEM-2100F (acceleration voltage of 200 kV). Images were acquired digitally on a Gatan multiople CCD camera. The UC emission spectra were taken on an F-4600 spectrophotometer equipped with an external tunable 1 W 980-nm laser diodes as the excitation source in place of the xenon lamp in the spectrometer. The emission split is 2.5 nm and the voltage of photomultiplier tube is 400 V. All the measurements were performed at room temperature.

3. Results and discussion

3.1. Structure, phase and morphology of the as-prepared products

In order to check compositions and phase purities of all products, the XRD was performed. Fig. 1 shows the XRD pattern of the YF_3:10%Yb^{3+}, 2%Er^{3+} precursor prepared via sonochemical route. It can be concluded that the positions of all diffraction peaks of the as-prepared YF_3:10%Yb^{3+}, 2%Er^{3+} precursor are in accordance with the standard data of YF_3 bulk, which was reported in JCPDS card with No. 74-0911. Moreover, no extra peaks from other phases are observed. Therefore, the as-prepared product is single phase of YF_3. It is worth to note that the diffraction peaks of the as-prepared precursor are remarkably broadened, which is owing to the small size effect of nanoparticles.

Fig. 2 shows the XRD patterns of $NaYF_4$:10%Yb^{3+}, 2%Er^{3+} powders prepared through hydrothermal process at 200 °C for various reaction times of (a) 2 h, (b) 7 h, (c) 20 h and (d) 24 h. As can been seen in Fig. 2(a), the diffraction peaks positions of product prepared through hydrothermal process at 200 °C at 2 h coincide with the

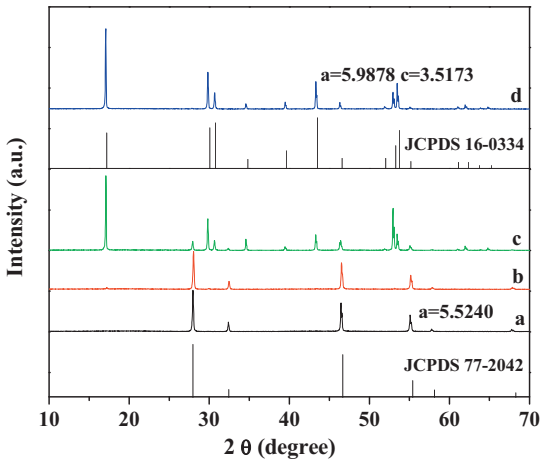

Fig. 2. XRD patterns of $NaYF_4$:10%Yb^{3+}/2%Er^{3+} products prepared though hydrothermal process at 200 °C for different reaction time, (a) 2 h, (b) 7 h, (c) 20 h, and (d) 24 h.

standard cubic phase $NaYF_4$ (JCPDS card No. 77-2042). No extra peaks from other phases are observed, which suggests that the pure cubic phase $NaYF_4$ can be prepared when YF_3 precursor solution was hydrothermally treated for 2 h. With increasing reaction time to 7 h, the new diffraction peaks from hexagonal phase $NaYF_4$ can be observed, which indicates that phase transition from cubic phase to hexagonal phase occurs (see in Fig. 2(b)). As shown in Fig. 2(c), the product mainly consists of hexagonal phase $NaYF_4$ when reaction time reaches to 20 h. At the moment, the content of cubic phase $NaYF_4$ is little. In Fig. 2(d), it can be found that when reaction time reaches to 24 h, the diffraction peaks of the product match very well with the pure hexagonal phase $NaYF_4$ which was reported in the JCPDS card with No. 16-0334. The cell parameters of the pure cubic and hexagonal phase $NaYF_4$:10%Yb^{3+}, 2%Er^{3+} crystals were also calculated by Jade 5.0 software. The cell parameters for cubic and hexagonal phase $NaYF_4$:10%Yb^{3+}, 2%Er^{3+} crystals are a = 5.5240 Å and a = 5.9878 Å, c = 3.5173 Å, respectively. In addition, in Fig. 2, it can also be seen that the diffraction peaks of all products are very sharp and strong, which indicates that the products with high crystallinity can be prepared by this method. This is important for phosphors, because high crystallinity generally means less traps and stronger luminescence.

The morphologies of the as-prepared YF_3:10%Yb^{3+}, 2%Er^{3+} precursor and $NaYF_4$:10%Yb^{3+}, 2%Er^{3+} samples were studied by FE-SEM. Fig. 3 shows typical FE-SEM images of the as-prepared YF_3:10%Yb^{3+}, 2%Er^{3+} precursor and $NaYF_4$:10%Yb^{3+}, 2%Er^{3+} samples, respectively. Among them images, Fig. 3(a and b) are low and high resolution FE-SEM images of the YF_3:10%Yb^{3+}, 2%Er^{3+} precursor prepared via sonochemical process, respectively. In Fig. 3(a), the homogeneous YF_3:10%Yb^{3+}, 2%Er^{3+} precursor submicrospindles are clearly observed. Their average diameter in the center is about 200 nm and length is about 600 nm. In order to further investigate the structure of YF_3:10%Yb^{3+}, 2%Er^{3+} submicrospindles, the high resolution FE-SEM was carried out. As shown in Fig. 3(b), it can be seen that every submicrospindle is composed of some nanoflakes with thickness of about 15 nm. These small sized nanoflakes structures lead remarkable broadening of XRD peaks. Fig. 3(c and d) presents the FE-SEM images of the products prepared via hydrothermal process for 2 h and 24 h, respectively. The morphologies of products with hydrothermal treatment are obviously different from that of the YF_3:10%Yb^{3+}, 2%Er^{3+} precursor. In Fig. 3(c), the uniform spherical cubic phase $NaYF_4$:10%Yb^{3+}, 2%Er^{3+} clusters were obtained when the YF_3:10%Yb^{3+}, 2%Er^{3+} precursor solution was hydrothermally treated for 2 h. The average diameter of cubic phase $NaYF_4$:10%Yb^{3+}, 2%Er^{3+} clusters is about 500 nm. In addition, we can also find that every cluster is composed of some spherical nanoparticles with about 100 nm in size. With increasing

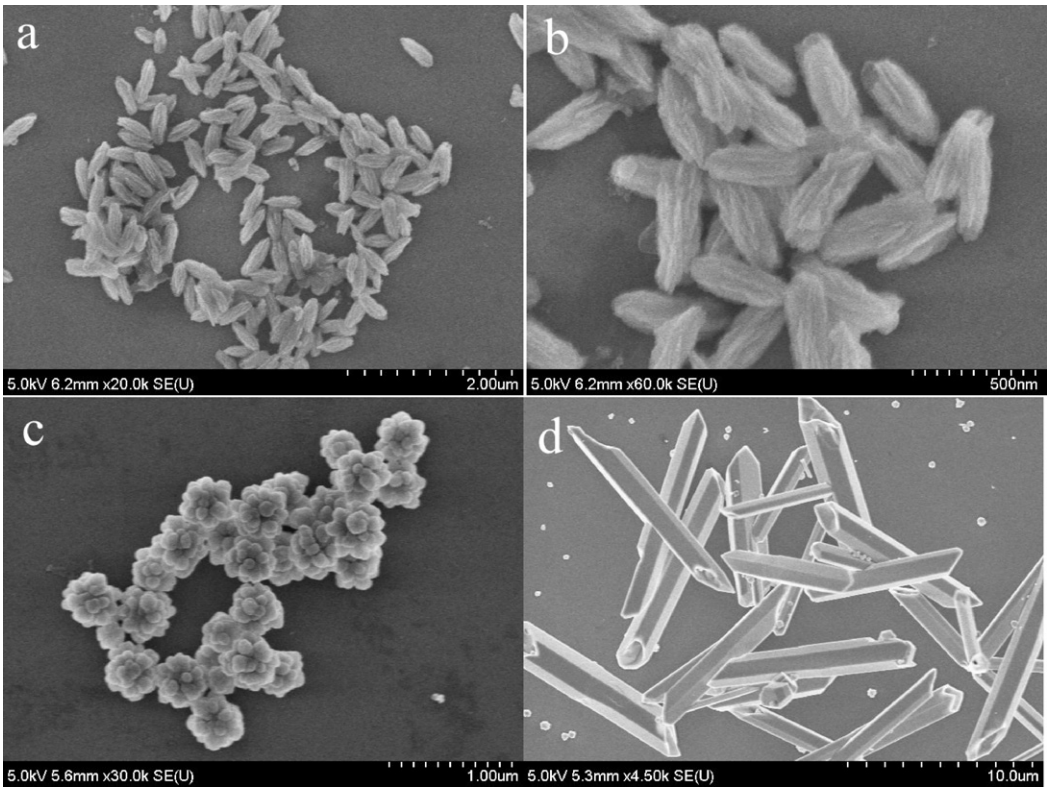

Fig. 3. FE-SEM images of the as-prepared YF_3:10%Yb^{3+}/2%Er^{3+} precursor and $NaYF_4$:10%Yb^{3+}/2%Er^{3+} products. (a–b) Low- and high resolution FE-SEM images of YF_3:10%Yb^{3+}/2%Er^{3+} precursor, (c) cubic phase $NaYF_4$:10%Yb^{3+}/2%Er^{3+}, and (d) hexagonal phase $NaYF_4$:10%Yb^{3+}/2%Er^{3+}.

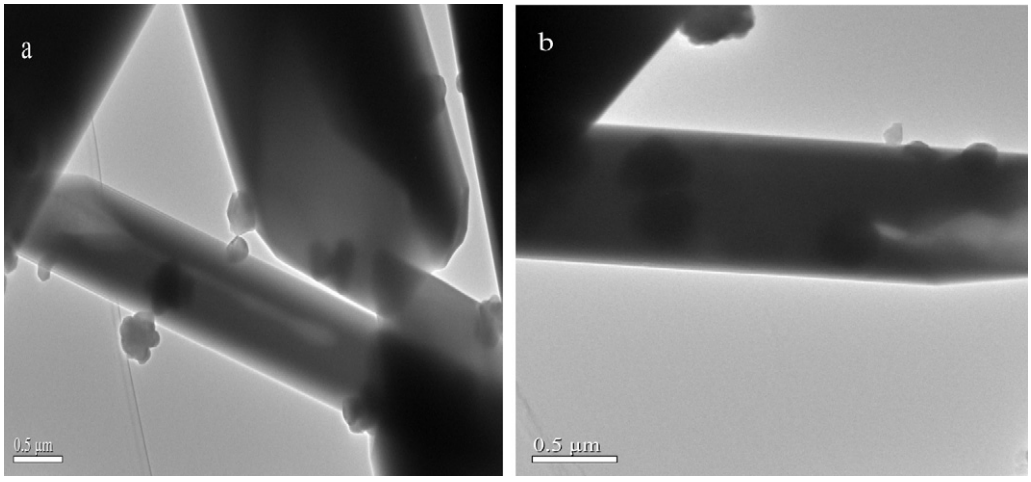

Fig. 4. TEM images of the as-prepared $NaYF_4$:10%Yb^{3+}/2%Er^{3+} prepared via hydrothermal process at 200 °C for 24 h.

hydrothermal reaction time, the morphology of product is greatly changed. Pure hexagonal phase $NaYF_4$:10%Yb^{3+}, 2%Er^{3+} were prepared when reaction time reached to 24 h. As shown in Fig. 3(d), the pure hexagonal phase $NaYF_4$:10%Yb^{3+}, 2%Er^{3+} sample consists of asymmetric hexagonal-prismatic tubular structures with out diameter of about 0.3–0.5 μm, inner diameter of about 0.5–1 μm and length ranging from 3 to 12 μm.

The insight into the microstructure of the samples can be obtained by further analysis of transmission electron microscopy (TEM) and HRTEM assays. Fig. 4 presents more details about inner structure of the hexagonal-prism microtubes. The hollow inner structure can be obviously observed from TEM images. The inner and out diameters of the microtubes are estimated to be 0.3–0.5 μm and 0.5–1 μm, which are consistent with the FE-SEM analysis. Furthermore, the microtubes with open end can be also clearly identified in Fig. 4(a and b). Therefore, the $NaYF_4$:10%Yb^{3+}, 2%Er^{3+} microtubes can be successfully prepared through this method.

3.2. Upconversion spectra

Upconversion luminescence (UCL) properties of the as-prepared spherical cubic phase $NaYF_4$:10%Yb^{3+}, 2%Er^{3+} clusters and hexagonal phase $NaYF_4$:10%Yb^{3+}, 2%Er^{3+} microtubes under 980-nm excitation were studied. Fig. 5 shows the UCL spectra of cubic phase $NaYF_4$:10%Yb^{3+}, 2%Er^{3+} clusters and hexagonal phase $NaYF_4$:10%Yb^{3+}, 2%Er^{3+} microtubes under 980-nm excitation, respectively. As shown in Fig. 5(a and b), the green emission band ranging from 510 to 570 nm and the red emission band ranging from 620 to 690 nm are clearly observed. The green emissions are attributed to the $^2H_{11/2}$, $^4S_{3/2} \rightarrow {}^4I_{15/2}$ transitions of Er^{3+} ions, and the red emission is ascribed to the $^4F_{9/2} \rightarrow {}^4I_{15/2}$ transition of Er^{3+} ions [24]. In addition, it also can be found that both green and red emissions of hexagonal phase are much stronger than that of cubic phase. In details, the intensity of green emissions of hexagonal phase is 10 times stronger than that of cubic phase, while the intensity of red emission of hexagonal phase is eight times stronger than that of cubic phase. These intense UC emissions and great improvement are mainly attributed to the following two aspects: On the one hand, it is well known that the phonon energy of host plays an important role in efficiency of UCL. It can also be confirmed that the lattice vibration energies of cubic and hexagonal phases $NaYF_4$ would be similar, that is to say the non-radiative transition rates of them would be approximately close. We believe that the deviation of UCL efficiency must be caused by the energy transfers efficiencies from Yb^{3+} to Er^{3+} or between Er^{3+} and the radiative transition rates of Er^{3+}, however, it is hard for us to give more detailed and specific supports on the above points from the present data. Meanwhile, the cubic phase is known to be about an order of magnitude less efficient than the corresponding hexagonal phase in the previous report [31]. On the other hand, in our work, the size of hexagonal phase microtubes are significantly larger than that of cubic phase clusters (500 nm) and the fraction of lanthanide ions near the surface of microtubes are much less than that of clusters, which can result in the decrease of nonradiative channels. Therefore, the UCL intensity and efficiency of hexagonal phase $NaYF_4$:10%Yb^{3+}, 2%Er^{3+} microtubes are much higher than that of cubic phase $NaYF_4$:10%Yb^{3+}, 2%Er^{3+} clusters.

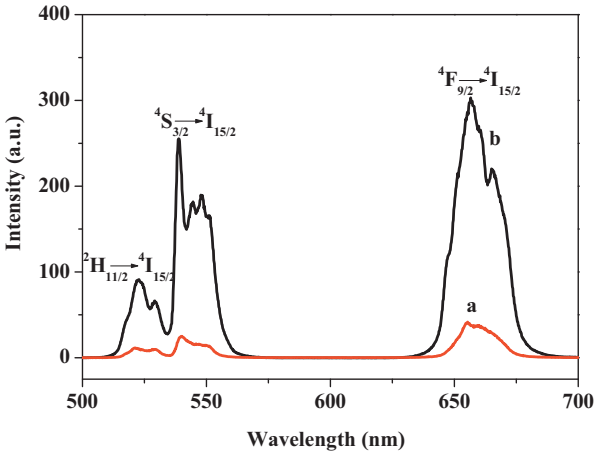

Fig. 5. UCL spectra of cubic and hexagonal phase of $NaYF_4$:10%Yb^{3+}/2%Er^{3+} under 980-nm laser diodes excitation with 1 W power. (a) Cubic phase and (b) hexagonal phase.

3.3. Power-dependent upconversion luminescence process

To better understand the mechanism of the green and red UCL, the dependence of green and red emissions intensities on the excitation power (input current) was performed. For any upconversion mechanism, the visible output intensity (I_v) is proportional to some power (n) of the infrared excitation power (I_{NR}) [38]:

$$I_v \propto I_{NR}^n \quad (1)$$

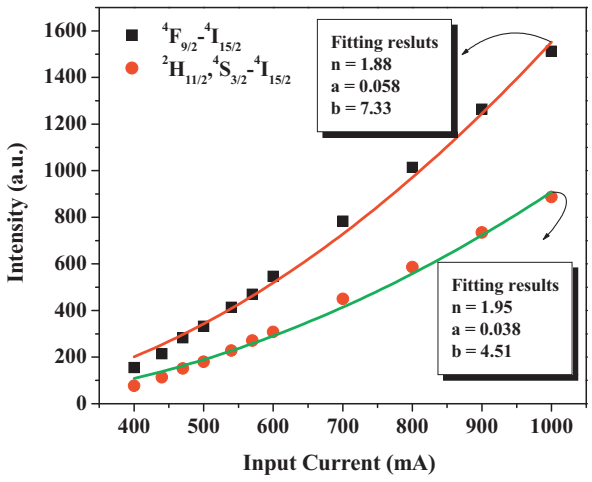

Fig. 6. Dependence of upconversion emission intensities on excitation power in hexagonal phase of $NaYF_4$:10%Yb^{3+}/2%Er^{3+} microtubes under 980-nm laser diodes excitation.

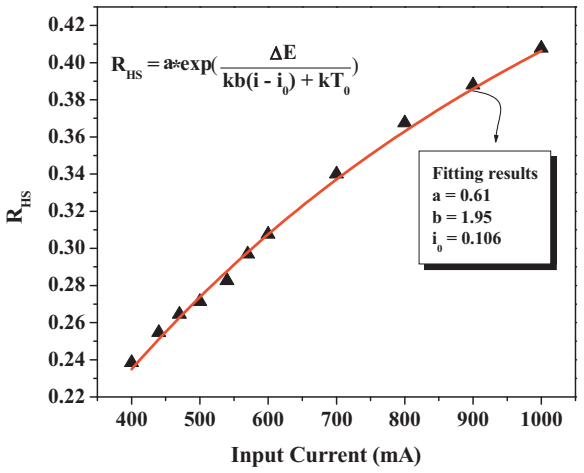

Fig. 7. Dependence of intensity ratio of $^2H_{11/2}$–$^4I_{15/2}$ to $^4S_{3/2}$–$^4I_{15/2}$ (R_{HS}) on the input current in $NaYF_4$:10%Yb^{3+}/2%Er^{3+} microtubes under 980-nm laser diodes excitation.

The relationship of excitation power (I_{NR}) and input current (i) can be written as follows:

$$I_{NR} = ai - b \quad (2)$$

Therefore, the visible output intensity can be also expressed as follows:

$$I_v \propto (ai - b)^n \quad (3)$$

Where a is constant, b/a is threshold current and n is the number of IR photon absorbed per visible photon emitted. The fitting results are shown in Fig. 6. The fitting n values are 1.95 and 1.88 for green and red emissions, respectively, which suggest that the two-photon process is involved for populating the green and red levels in the UC process. The fitting results for spherical cubic phase $NaYF_4$:10%Yb^{3+}, 2%Er^{3+} clusters also indicate that the UCL involves a two-photon absorption process. These results also suggest that structure of phase has no effect on the UCL mechanism.

It is worth while to note the intensity ratio (R_{HS}) of $^2H_{11/2} \rightarrow {}^4I_{15/2}$ to $^4S_{3/2} \rightarrow {}^4I_{15/2}$ emissions of Er^{3+} ions, which represents the temperature of sample under the excitation of 980 nm. For Er^{3+} ions, the energy separation between the two nearest excited states $^2H_{11/2}$ and $^4S_{3/2}$ is only several hundred wavenumbers. As the down $^4S_{3/2}$ level is populated, immediately the upper $^2H_{11/2}$ level is thermal populated owing to Boltzmann's distribution. This will lead the intensity ratio R_{HS} to be sensitive to temperature. Therefore, R_{HS} is a critical parameter to study thermal effect in $NaYF_4$:10%Yb^{3+}, 2%Er^{3+} microtubes under the exposure of the 980-nm laser diode. Fig. 7 shows R_{HS} as a function of input current in $NaYF_4$:10%Yb^{3+}, 2%Er^{3+} microtubes. It is obvious that with the increase of input current, the value of R_{HS} was increased. This is understood easily. When the input current or the excitation power increased, more 980-nm photons were absorbed, leading the temperature to increase more. According to Boltzmann's distribution, R_{HS} as a function of temperature can be written as [39]

$$R_{HS} = \frac{I_{2H_{11/2}}}{I_{4S_{11/2}}} = \alpha e^{-\Delta E/kT} \quad (4)$$

where α is a constant, ΔE is the energy separation between the $^2H_{11/2}$ and the $^4S_{3/2}$ levels (700 cm^{-1}), k is Boltzmann's constant, and T is the absolute temperature. In our previous results, we found that the temperature of sample is proportional to the input current of the laser diode [40]. Therefore, R_{HS} also can be expressed as:

$$R_{HS} = \alpha e^{-\Delta E/kb(i-i_0)+kT_0} \quad (5)$$

In Eq. (5), b is a constant and T_0 is room temperature. The data in Fig. 7 were well fitted by using Eq. (5). In the fitting process, the threshold current, i_0, was deduced to be 0.106 A, which is consistent with that derived from Fig. 6 ($b/a \approx 0.130$ A). This result suggests that this model can well explain the relationship between the intensity ratio of R_{HS} and the working current of laser diodes.

Fig. 8 shows the energy-level diagram of Yb^{3+}/Er^{3+} co-doped $NaYF_4$ and population processes under 980-nm excitation. In Er^{3+} and Yb^{3+} co-doped systems, the UC process occurs via two successive energy transfers (ET) from the Yb^{3+} ion to the Er^{3+} ion [24]. Following 980-nm irradiation, firstly, Er^{3+} ions in the ground states are excited to $^4I_{11/2}$ states via ET of neighboring Yb^{3+} and Er^{3+}. Subsequently, nonradiative relaxation of $^4I_{11/2} \rightarrow {}^4I_{13/2}$ also populates the $^4I_{13/2}$ level [38]. In the bulk $NaYF_4$, the maximum phonon energy is about 370 cm^{-1} [41], which is much smaller than the energy gaps of $^4I_{11/2}$ and $^4I_{13/2}$. According to the theory of multiphonon relaxation, the nonradiative relaxation probability of $^4I_{11/2} \rightarrow {}^4I_{13/2}$ is relatively small, which results in the weak red emission [42]. However, the intensity of red emission is stronger than that of green emissions in our experiment. The reason may be explained as follows. (1) The surface of material absorbs a large number of high-energy vibration modes such as OH^- and

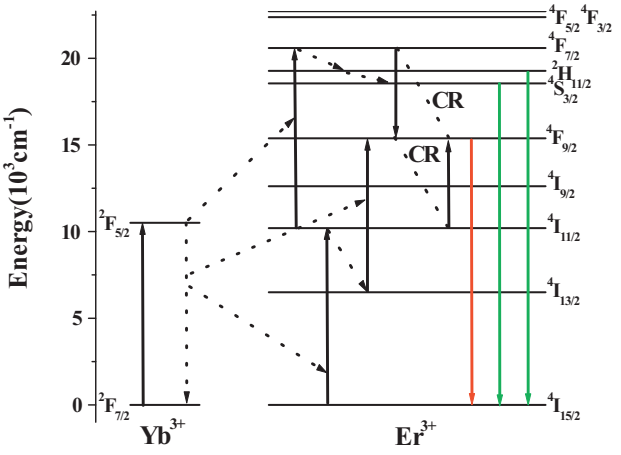

Fig. 8. Energy level diagram and transition processes of hexagonal phase of $NaYF_4$:10%Yb^{3+}/2%Er^{3+} microtubes under 980-nm laser diodes excitation.

CO_3^{2-} groups. Few high-energy phonons can easily bridge the gap between the $^4I_{11/2}$ and $^4I_{13/2}$ states and the probability of multi-phonon relaxation is rather large. (2) The other reason is that 2 mol% of Er^{3+} doped concentration, which is relatively high, leads to the cross-relaxation (CR) process of $^4F_{7/2} \rightarrow {}^4F_{9/2}$ and $^4I_{11/2} \rightarrow {}^4F_{9/2}$ between the two nearby Er^{3+} ions [43]. These reasons both increase the population of the $^4F_{9/2}$ level. Therefore, the intensity of red emission is stronger than that of green emissions. In the second-step excitation, the same laser pumps the excited state atoms from the $^4I_{11/2}$ level to the $^4F_{7/2}$ level via ET and excited-state absorption (ESA), or from the $^4I_{13/2}$ state to the $^4F_{9/2}$ state via phonon-assisted ET. Subsequent nonradiative relaxations of $^4F_{7/2} \rightarrow {}^4S_{3/2}$ and $^4F_{7/2} \rightarrow {}^4F_{9/2}$ populate the $^4S_{3/2} \rightarrow {}^2H_{11/2}$ as well as the $^4F_{9/2}$ states. As a consequence, the two-photon green emissions of $^4S_{3/2}$, $^2H_{11/2} \rightarrow {}^4I_{15/2}$ and the red emission of $^4F_{9/2} \rightarrow {}^4I_{15/2}$ occur. The two-photon process for red UC emission can be expressed as following formulas:

(1) $^4I_{15/2}$ (Er^{3+}) + $^2F_{5/2}$ (Yb^{3+}) → $^4I_{11/2}$ (Er^{3+}) + $^2F_{7/2}$ (Yb^{3+}) (energy transfer)
(2) $^4I_{11/2}$ (Er^{3+}) → $^4I_{13/2}$ (Er^{3+}) (nonradiative relaxation)
(3) $^4I_{13/2}$ (Er^{3+}) + $^2F_{5/2}$ (Yb^{3+}) → $^4F_{9/2}$ (Er^{3+}) + $^2F_{7/2}$ (Yb^{3+}) (energy transfer)
(4) $^4F_{9/2}$ (Er^{3+}) → $^4I_{15/2}$ (red emission)

The two-photon process for green UC emission can be expressed as follows:

(1) $^4I_{15/2}$ (Er^{3+}) + $^2F_{5/2}$ (Yb^{3+}) → $^4I_{11/2}$(Er^{3+}) + $^2F_{7/2}$ (Yb^{3+}) (energy transfer)
(2) $^4I_{11/2}$ (Er^{3+}) + $^2F_{5/2}$ (Yb^{3+}) → $^4F_{7/2}$ (Er^{3+}) + $^2F_{5/2}$ (Yb^{3+}) (energy transfer)
(3) $^4F_{7/2}$ (Er^{3+}) → $^2H_{11/2}$(Er^{3+}) → $^4S_{3/2}$(Er^{3+}) (nonradiative relaxation)
(4) $^2H_{11/2}$, $^4S_{3/2}$ (Er^{3+}) → $^4I_{15/2}$ (green emissions)

4. Conclusions

In conclusion, spherical cubic phase $NaYF_4$:10%Yb^{3+}, 2%Er^{3+} clusters and hexagonal phase $NaYF_4$:10%Yb^{3+}, 2%Er^{3+} microtubes have been successfully synthesized through hydrothermal processes with YF_3:10%Yb^{3+}, 2%Er^{3+} submicrospindles as precursor. The hydrothermal treatment time plays a crucial role in the control of structure, phase and morphology of the final product. The results indicate that the phase transition from cubic phase to hexagonal phase occurs with the increase of reaction time. Moreover, the morphological evolvement of product also can be observed from spherical clusters to microtubes with the increase of reaction time. Comparing with the cubic phase Yb^{3+}/Er^{3+} co-doped $NaYF_4$ clusters, hexagonal phase microtubes exhibit the much higher UCL efficiency. Therefore, it is expected that these tubular structured $NaYF_4$ with much stronger UCL efficiency will have potential application in photonic device.

Acknowledgments

This work was partially supported by Foundation of Education Department of Liaoning Province (Grant No. 2009A148), Fundamental Research Funds for the Central Universities (Grant No. DC10020105 and 017004) and NSFC (National Natural Science Foundation of China, grant Nos. 50972021 and 61078061).

References

[1] H. Li, R. Liu, R.X. Zhao, Y.F. Zheng, W.X. Chen, Z.D. Xu, Cryst. Growth Des. 6 (2006) 2795.
[2] X.F. Guan, L.P. Li, G.S. Loi, Z.W. Fu, J. Zheng, T.J. Yan, J. Alloys Compd. 509 (2011) 3367.
[3] J.X. Liu, X.L. Dong, X.W. Liu, F. Shi, S. Yin, T. Sato, J. Alloys Compd. 509 (2011) 1482.
[4] Y.M. Wang, H.F. Liu, M. Bao, B.J. Li, H.F. Su, Y.X. Wen, F. Wang, J. Alloys Compd. 509 (2011) 1482.
[5] Z.G. Chen, Q.W. Tian, Y.L. Song, J.M. Yang, J.Q. Hu, J. Alloys Compd. 506 (2010) L17.
[6] S.L. Zhong, J.J. Chen, S.P. Wang, Q.Y. Liu, Y.L. Wang, S.L. Wang, J. Alloys Compd. 493 (2010) 322.
[7] X.X. Ji, X.T. Huang, J.P. Liu, J. Jiang, X. Li, R.M. Ding, Y.Y. Hu, F. Wu, J. Alloys Compd. 503 (2010) L21.
[8] C.R. Li, M.Y. Cui, Q.T. Sun, W.J. Dong, Y.Y. Zheng, K. Tsukamoto, B.Y. Chen, W.H. Tang, J. Alloys Compd. 504 (2010) 498.
[9] T. Xia, J.P. Wang, N. Lin, L.H. Huo, H. Zhao, G. Mountrichas, J. Alloys Compd. 507 (2010) 245.
[10] Y. Tian, B.J. Chen, B.N. Tian, R.N. Hua, J.S. Sun, L.H. Cheng, H.Y. Zhong, X.P. Li, J.S. Zhang, Y.F. Zheng, T.T. Yu, L.B. Huang, Q.Y. Meng, J. Alloys Compd. 509 (2011) 6096.
[11] Y. Tian, B.J. Chen, H.Q. Yu, R.N. Hua, X.P. Li, J.S. Sun, L.H. Cheng, H.Y. Zhong, J.S. Zhang, Y.F. Zheng, T.T. Yu, L.B. Huang, J. Colloid Interface Sci. 360 (2011) 586.
[12] H. Li, W.J. Li, L. Ma, W.X. Chen, J.M. Wang, J. Alloys Compd. 471 (2009) 442.
[13] L.H. Shen, T.M. Cheng, L.J. Wu, X.F. Li, Q.L. Cui, J. Alloys Compd. 465 (2008) 245.
[14] L. Yang, W.S. Guan, B. Bai, Q. Xu, Y. Xiang, J. Alloys Compd. 504 (2010) L10.
[15] M. Knez, A.M. Bittner, F. Boes, C. Wege, H. Jeske, E. Maib, K. Kern, Nano Lett. 3 (2003) 1079.
[16] A.L. Litvin, S. Valiyaveettil, D.L. Kaplan, S. Mann, Adv. Mater. 9 (1997) 124.
[17] L. Yang, L.Q. Zhou, X.G. Chen, X.L. Liu, P. Hua, Y. Shi, X.G. Yue, Z.W. Tang, Y. Huang, J. Alloys Compd. 509 (2011) 3866.
[18] Q. Sun, X.Q. Chen, Z.K. Liu, F.P. Wang, Z.H. Jiang, C. Wang, J. Alloys Compd. 509 (2011) 5336.
[19] Y.V. Yermolayeva, A.T. Tolmachev, M.V. Dobrotvorskaya, O.M. Vovk, J. Alloys Compd. 509 (2011) 5320.
[20] N. Niu, P.P. Yang, Y. Wang, W.X. Wang, F. He, S.L. Gai, D. Wang, J. Alloys Compd. 509 (2011) 3096.
[21] C.X. Li, Z.Y. Hou, C.M. Zhang, P.P. Yang, G.G. Li, Z.H. Xu, Y. Fan, J. Lin, Chem. Mater. 21 (2009) 4598.
[22] Y. Tian, X.H. Qi, X.W. Wu, R.N. Hua, B.J. Chen, J. Phys. Chem. C 113 (2009) 10767.
[23] H. Lin, D.Q. Chen, Y.L. Yu, Z.F.P. Huang, A.P. Yang, Y.S. Wang, J. Alloys Compd. 509 (2011) 3363.
[24] J.Y. Sun, J.B. Xian, X.Y. Zhang, H.Y. Du, J. Alloys Compd. 509 (2011) 2348.
[25] J.A. Capobianco, G. Prevost, P.P. Proulx, P. Kabro, M. Bettinelli, Opt. Mater. 6 (1996) 175.
[26] A.S. Oliveira, M.T. de Araujo, A.S. Gouveia-Neto, A.S.B. Sombra, J.A. Medeiros Neto, N. Aranha, J. Appl. Phys. 83 (1998) 604.
[27] A.S. Oliveira, M.T. de Araujo, A.S. Gouveia-Neto, J.A. Medeiros Neto, A.S.B. Sombra, Y. Messaddeq, Appl. Phys. Lett. 72 (1998) 753.
[28] P.V. dos Santos, E.A. Gouveia, M.T. de Araujo, A.S. Gouveia-Neto, A.S.B. Sombra, J.A. Medeiros Neto, Appl. Phys. Lett. 74 (1999) 3607.
[29] A.S. Gouveia-Neto, E.B. da Costa, L.A. Buenob, S.J.L. Ribeiro, J. Alloys Compd. 375 (2004) 224.
[30] A.S. Gouveia-Neto, E.B. da Costa, L.A. Buenob, S.J.L. Ribeiro, J. Lumin. 110 (2004) 79.
[31] K.W. Kramer, D. Biner, G. Frei, H.U. Gudel, M.P. Hehlen, S.R. Luthi, Chem. Mater. 16 (2004) 1244.
[32] Y. Xia, P. Yang, Y. Sun, Y. Wu, B. Mayers, B. Gates, Y. Yin, F. Kim, H. Yan, Adv. Mater. 15 (2003) 353.
[33] F. Krumeich, H.J. Muhr, M. Niederberger, F. Bieri, B. Schnyder, R. Nesper, J. Am. Chem. Soc. 121 (1999) 8324.
[34] Q. Wu, Z. Hu, X.Z. Wang, Y.N. Lu, X. Chen, H. Xu, Y. Chen, J. Am. Chem. Soc. 125 (2003) 10176.
[35] Q.Y. Lu, F. Gao, D.Y. Zhao, Nano Lett. 2 (2002) 725.
[36] F. Zhang, Y. Wan, T. Ying, F.Q. Zhang, Y.F. Shi, S.H. Xie, Y.G. Li, L. Xu, B. Tu, D.Y. Zhao, Angew. Chem. Int. Ed. 46 (2007) 7976.
[37] F. Zhang, D.Y. Zhao, ACS Nano 3 (2009) 159.
[38] F. Vetrone, J.C. Boyer, J.A. Capobianco, J. Appl. Phys. 96 (2004) 661.
[39] X. Bai, H.W. Song, G.H. Pan, Y.Q. Lei, T. Wang, X.G. Ren, S.Z. Lv, B. Dong, Q.L. Dai, L.B. Fan, J. Phys. Chem. C 111 (2007) 13611.
[40] W.L. Lu, L.H. Cheng, H.Y. Zhong, J.S. Sun, J. Wan, Y. Tian, B.J. Chen, J. Phys. D: Appl. Phys. 43 (2010) 085404.
[41] J.F. Suyver, J. Grimm, M.K. Van Veen, D. Biner, K.W. Krämer, H.U. Güdel, J. Lumin. 117 (2006) 1.
[42] C.B. Layne, W.H. Lowdermilk, M.J. Weber, Phys. Rev. B 16 (1997) 10.
[43] J.W. Zhao, Y.J. Sun, X.G. Kong, L.J. Tian, Y. Wang, L.P. Tu, J.L. Zhao, H. Zhang, J. Phys. Chem. B 112 (2008) 15666.